OPEN ACCESS
IOP Publishing | Songshan Lake Materials Laboratory Materials Futures
Mater. Futures 1 (2022) 045101 (12pp) https://doi.org/10.1088/2752-5724/ac9707

Defect passivation and electrical conductivity enhancement in perovskite solar cells using functionalized graphene quantum dots

Yichuan Rui[1,*], Zuoming Jin[1], Xinyi Fan[1], Weitao Li[2], Bin Li[1], Tianpeng Li[1,3], Yuanqiang Wang[1], Liang Wang[2,*] and Jia Liang[3,*]

[1] College of Chemistry and Chemical Engineering, Shanghai University of Engineering Science, Shanghai 201620, People's Republic of China
[2] Institute of Nanochemistry and Nanobiology, School of Environmental and Chemical Engineering, Shanghai University, Shanghai 200444, People's Republic of China
[3] Department of Materials Science, Fudan University, 220 Handan Road, Shanghai 200433, People's Republic of China

E-mail: ryc713@126.com, wangl@shu.edu.cn and jialiang@fudan.edu.cn

Received 25 June 2022, revised 2 October 2022
Accepted for publication 3 October 2022
Published 21 October 2022

Abstract

Organic–inorganic halide perovskites have been intensively investigated as potential photovoltaic materials due to their exceptional optoelectronic properties and their successful applications in perovskite solar cells (PSCs). However, a large number of defect states still exist in the PSCs so far and are detrimental to their power conversion efficiencies (PCEs) and stability. Here, an effective strategy of incorporating single-crystalline graphene quantum dots (GQDs) into the perovskite films is proposed to passivate the defect states. Intriguingly, the GQD-modified perovskite films exhibit purer phase structure, higher quality of morphology, and higher electrical conductivity when compared with the control perovskite films. All of the advantages caused by the incorporation of the GQDs lead to fast carrier separation and transport, long carrier lifetime, and low nonradiative recombination in the PSCs based on the GQD-modified perovskite films. As a result, this kind of PSC displays an increase in all photovoltaic parameters, and its PCE shows an enhancement of more than 20% when compared with the control PSC. Moreover, this novel PSC is demonstrated to have long-term stability and resistibility against heat and moisture. Our findings provide an insight into how to passivate the defect states and enhance the electrical conductivities in the perovskites and pave the way for their further exploration to achieve higher photovoltaic performances.

Supplementary material for this article is available online

Keywords: perovskite solar cells, graphene quantum dots, defect passivation, electrical conductivity enhancement, recombination rate

* Authors to whom any correspondence should be addressed.

Future perspectives
Based on their excellent optoelectronic properties, facile and low-temperature solution process, and low cost, organic–inorganic metal halide perovskite solar cells (PSCs) have become a rising star for the next-generation photovoltaics. A large number of advances have been achieved in the PSCs so far, however, the existence of various defects is still one of the big stumbling blocks for their rapid development. Here, we incorporated the graphene quantum dots (GQDs) with functional groups into the perovskite films to passivate their defect states. As a result, the defect densities in the perovskite films were reduced dramatically. Moreover, different from the polymeric passivator as reported previously, the GQDs also endowed the perovskite film with excellent electrical conductivity, which is beneficial for the carrier transport. In short, our findings provide a more effective strategy to design passivators and open the door for further improving the efficiency and stability of the PSCs.

1. Introduction

Perovskite solar cells (PSCs) have aroused worldwide attentions due to the explosive growth rate of the power conversion efficiency (PCE) originating from their high extinction coefficient, low exciton binding energy and fast charge diffusion rate [1–3]. It is well known that the low-temperature solution process is one of the critical advantages for the PSCs when compared with other traditional semiconductor photovoltaic devices [4–9]. However, as the solution process is far from thermodynamic equilibrium, a large number of defect states inevitably exist within the polycrystalline perovskite film, such as anion/cation vacancies, antisite occupations, and interstitials [10–12]. These defects detrimentally act as nonradiative recombination sites, resulting in poor charge transport, severe ion migration, instability, and other shortcomings [13, 14]. In order to resolve these problems, tremendous efforts have been devoted, for instance, post-annealing treatment of $MAPbI_3$ perovskite films with methylamine effectively reduces the surface/interface defects [15]; the optimization of device structure could mitigate the defect induced ion migration [16]. The grain boundaries in perovskite film are currently considered to be responsible for causing recombination and trapping of charge carriers [17]. The importance of grain boundary passivation has been recognized, some effective approaches have been developed [18–20], such as adding excess PbI_2/MAI in the precursors [21, 22] or introducing polymer additives [23–27] into the perovskite films to passivate the trap states. These approaches, however, exhibited inferior reproducibility and electrical conductance because of the demanding experimental conditions and intrinsic nonconductive characteristics of the polymers. Therefore, it is imperative for us to explore new strategies to passivate the defect states in the perovskites and then enhance the PCEs and stability of the PSCs.

Graphene quantum dots (GQDs), an intriguing low-dimensional material, possess high conductivity, quantum size effect, superior optical properties, and other virtues [28, 29]. Moreover, the rich functionalized groups in GQDs deriving from the synthetic conditions, such as hydroxyl (−OH), carbonyl (−C=O), carboxylic (–COOH) and amine ($-NH_2$), endow them with various applications [30, 31]. Recently, carbonaceous materials including carbon nanodots [32, 33], graphdiyne [34] and fullerenes [35] were successfully employed in the PSCs as the passivators, which showed positive effects on reducing their nonradiative recombination rates and prolonging their carrier lifetime. Compared with these carbonaceous materials, GQDs show much better crystallinity and fewer defects due to their large homogeneous conjugated domains [36]. Moreover, the terminal functional groups in GQDs could passivate the trap states in the perovskite films, meanwhile the benign conductivity could facilitate the charge transport across the whole perovskite films. Following this line of thought, a perovskite composite film, incorporating GQDs into the $MAPbI_3$ perovskite, was fabricated by a dynamic two-step spin-coating process in this work. In order to avoid the aggregation, the concentrated GQDs solution was directly added into the PbI_2/*N*,*N*-Dimethylformamide (DMF) precursor. As expected, a low defect density was demonstrated in the GQD-modified $MAPbI_3$ perovskite film, and it also possessed a high electrical conductivity, pure phase structure and high-quality morphology. All of the advantages endowed the GQD-modified $MAPbI_3$ perovskite film with fast carrier separation and transport, long carrier lifetime, and low nonradiative recombination. As a result, the GQD-modified $MAPbI_3$-based PSC showed an improvement of more than 20% in the PCE when compared with the pristine $MAPbI_3$-based PSC. Moreover, this new PSC exhibited good long-term stability and resistibility against heat and moisture as well.

2. Methods

2.1. Synthesis and purification of GQDs

The single-crystalline GQDs were synthesized by a mild and green hydrothermal method. In brief, 2 g pyrene was nitrated into trinitropyrene in hot HNO_3 (160 ml) at 80 °C and then stirred for 12 h. Then, the mixture was diluted with deionized water. 3 g resultant 1,3,6-trinitropyrene was dispersed in the NaOH solution and ultrasonicated for 3 h. The suspension was then transferred to a Teflon lined autoclave and kept at 200 °C for 10 h. After cooling to room temperature, the water-soluble GQDs were further dialyzed in a dialysis bag for 2 d to remove impurities, such as sodium salts and unfused small molecules. The as-obtained GQDs aqueous dispersion showed a high concentration of about 10 mg ml^{-1}.

2.2. Electrode preparation

Fluorine doped tin oxide (FTO) glass was firstly etched by Zn powder and HCl solution, and then ultrasonically cleaned in detergent solution, deionized water and ethanol for 20, 15 and 15 min, respectively. A compact TiO_2 layer was deposited on the FTO substrate by spin coating at 4000 rpm for 30 s and calcined at 500 °C for 30 min in air. Subsequently, a mesoporous TiO_2 layer was deposited on the compact TiO_2 layer by spin coating at 4000 rpm for 30 s. The layer was dried at

100 °C for 10 min and then sintered at 500 °C for 30 min in air again. Before each spin-coating step, the substrates were treated with Ultraviolet-O_3 for 30 min to remove organic residuals and increase surface wetting properties.

2.3. Fabrication of PSCs

The fabrication process of the PSCs has been described in our previous works [37–39]. Firstly, the GQDs were diluted in DMF with concentrations of 0.001, 0.005 and 0.01 g ml^{-1}, and 1.0 M PbI_2 was added into the DMF or DMF/GQDs to prepare the PbI_2 precursor solution. Meanwhile, 0.3 M methylammonium iodide (MAI) was added into isopropanol to prepare the MAI precursor solution. The $MAPbI_3$ perovskite layers were deposited onto the substrates by a specially designed dynamic two-step spin-coating method, which combines the merits of one-step antisolvent deposition and two-step sequential deposition. Specifically, 40 μl PbI_2 or PbI_2/GQDs precursor solution was dripped on the substrate and then spin-coated at 3000 rpm for 30 s. During this step at 10 s, 50 μl MAI precursor solution was immediately dripped on the PbI_2 or PbI_2/GQDs layer to form the perovskite layer. The perovskite layer was subsequently annealed at 70 °C for 30 min and 150 °C for 20 min, respectively. Spiro-OMeTAD solution was spin-coated on the perovskite film at 4000 rpm for 10 s as the hole transport layer. Finally, an 80 nm thick Au electrode was deposited by the thermal evaporation method through an aperture mask (0.16 cm^2 for each sub-cell) to pattern the electrodes.

3. Results

GQDs were synthesized by a bottom-up hydrothermal method using the nitrated pyrene molecule as the precursor. Figure 1(a) shows the photographs of the as-synthesized GQD solution under different conditions, which reveals the GQDs disperse in water uniformly and exhibits green-yellow fluorescence under the illumination of 365 nm ultraviolet light. The steady state photoluminescence (PL) spectra of the GQDs/DMF solution (1 mg ml^{-1}) under different excitation wavelengths were investigated, as shown in figure S1. As the excitation wavelength increases from 350 to 450 nm, the emission peaks show a slightly red shift from 550 to 560 nm, which implies the GQDs possess defect-free single-crystalline structures and ideal electron donating functionalization at edge sites according to previous reports [40, 41]. This result is also echoed by the high-resolution transmission electron microscope (HRTEM) image, as shown the inset in figure 1(b), in which few misalignments of lattice structures can be found in such high resolution. Moreover, the HRTEM image also displays the distinct lattice fringe with a spacing of 0.21 nm, which corresponds to (100) plane of graphene. In order to identified the sizes of the GQDs, TEM and atomic force microscope (AFM) measurements were carried out. The TEM image in figure 1(b) shows that the lateral sizes of the GQDs distribute over a narrow range with an average lateral size of 2.5 nm. Meanwhile, the altitude intercept in the AFM image of 1.4 nm demonstrates that the as-prepared GQDs have the uniform thicknesses and the number of layers is 4–5, as shown in figure 1(c). Figure S2 displays the Fourier transform infrared spectroscopy spectrum of the GQD powder. The strong vibrations around 1584 cm^{-1}, 3353 cm^{-1}, and 1268 cm^{-1} can be ascribed to the C=C bond, O–H bond, and C–O–H bond, respectively. Such functional groups can provide meaningful interaction with the perovskites, especially for their unbonded Pb^{2+} and I^- ions, which will be very helpful for passivating these defects.

In order to demonstrate the effects of the GQDs on the perovskite materials, $MAPbI_3$, GQD-modified $MAPbI_3$ perovskite films with different concentrations of GQDs were prepared, as shown in figure 1(f). The fabrication process was described in the Methods. The GQD-modified $MAPbI_3$ perovskite films are hereafter referred to as $MAPbI_3$/xGQDs, where x is the concentration of the GQD solution. In order to verify the incorporation of GQDs in the $MAPbI_3$ perovskite films successfully, Raman spectra of the $MAPbI_3$ and $MAPbI_3$/xGQDs ($x = 0.001$, 0.005, and 0.01) perovskite films were measured, as shown in figure 2(a). No peaks can be found in the $MAPbI_3$ film, while the $MAPbI_3$/xGQDs ($x = 0.001$, 0.005, and 0.01) films display obvious two peaks at 1373 and 1576 cm^{-1}, corresponding to the disordered D-band and the crystalline G-band of GQDs, respectively, which demonstrates that the GQDs were incorporated into the $MAPbI_3$ perovskite films successfully [42, 43]. Moreover, the intensities of G-bands are much stronger than those of the D-bands in the $MAPbI_3$/xGQDs ($x = 0.001$, 0.005, and 0.01) perovskite films, which suggests that the crystallinities of the GQDs in these perovskite films are high. In order to examine the interaction between $MAPbI_3$ and GQDs, the x-ray photoelectron spectroscopy (XPS) spectra of the $MAPbI_3$ and $MAPbI_3$/xGQDs ($x = 0.001$, 0.005, and 0.01) perovskite films were performed. Figure 2(b) shows wide scan XPS survey, which demonstrates that all of signals of the Pb 4f, C 1s, N 1s, O 1s, and I 3d peaks can be found in the four kinds of perovskite films. Figures 2(c) and (d) further show the high-resolution XPS spectra of the Pb 4f and I 3d, respectively. The Pb 4f core level displays two main peaks corresponding to Pb $4f_{7/2}$ and $4f_{5/2}$ due to the spin-orbital splitting. The peaks in $MAPbI_3$ film are located at 137.1 and 142.0 eV, which show around 0.2 eV higher than those in $MAPbI_3$/xGQDs ($x = 0.001$, 0.005, and 0.01) perovskite films. These shifts can be ascribed to the changes of chemical bonding. Therefore, it is deduced that the incorporated GQDs generate an increased electron cloud density around the Pb and I atoms due to the strong interaction between GQDs and perovskites [33].

Figure 2(e) shows the x-ray diffraction patterns of the $MAPbI_3$ and $MAPbI_3$/xGQDs ($x = 0.001$, 0.005, and 0.01) perovskite films. The diffraction peaks at 14.2°, 19.9°, 23.4°, 24.5°, 28.4°, 31.9°, 40.6° and 43.2° are correlated to the (110), (112), (211), (202), (220), (310), (224) and (314) planes of the tetragonal $MAPbI_3$, respectively. As compared with the $MAPbI_3$ film, no peak shift is observed for the $MAPbI_3$/xGQDs ($x = 0.001$, 0.005, and 0.01) perovskite films, implying that the incorporated GQDs would not affect the lattice structure of the $MAPbI_3$ film [44]. It is well known that

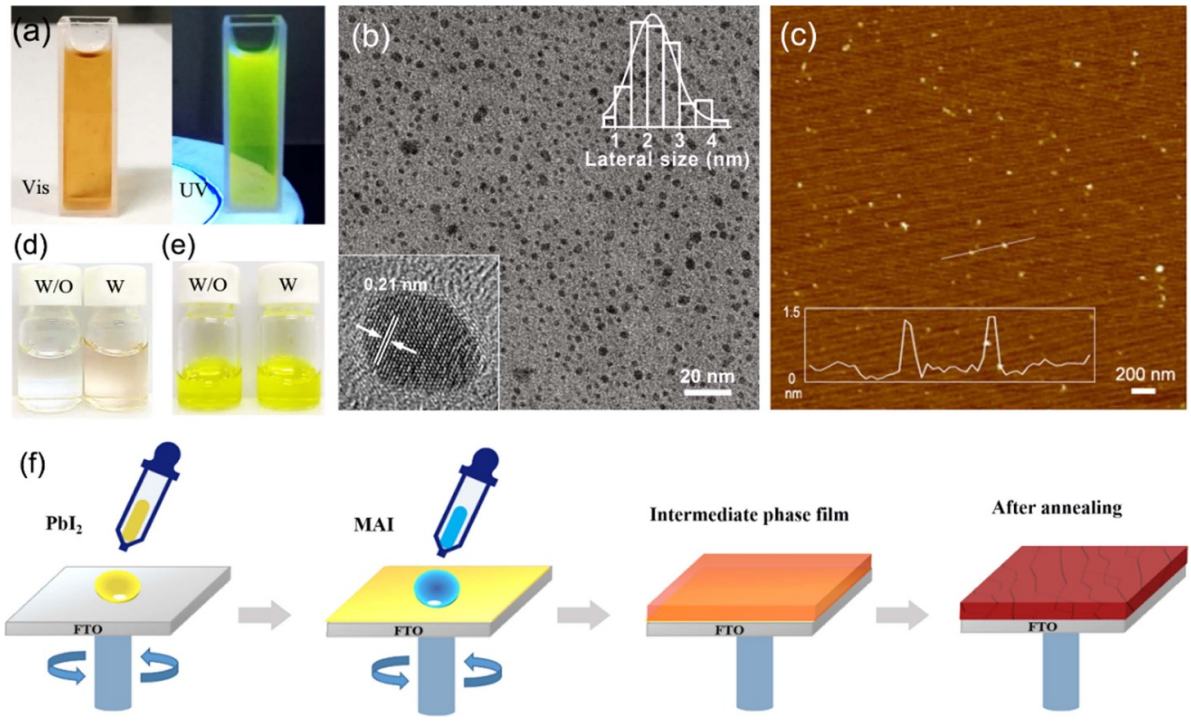

Figure 1. (a) Typical digital pictures of the GQD solution under the illumination of visible and 365 nm ultraviolet light, respectively. (b) TEM and HRTEM images of the GQDs. The inset shows the lateral size distribution. (c) AFM image of the GQDs. The inset shows the corresponding height profile. Digital pictures of (d) DMF solution and (e) PbI_2/DMF solution with and without GQDs, respectively. (f) Fabrication process of GQD-modified perovskite films using the dynamic two-step spin-coating method.

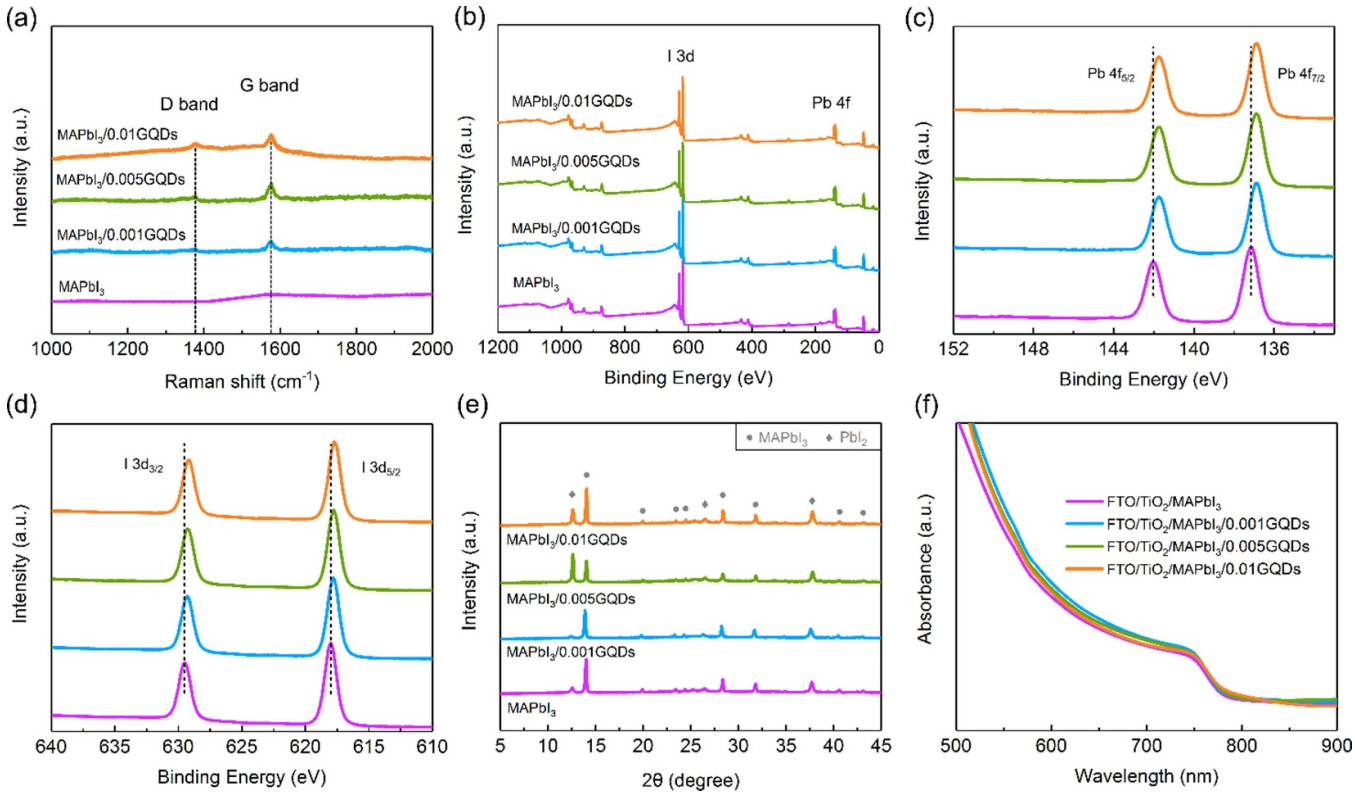

Figure 2. (a) Raman spectra, (b) XPS survey spectra, high-resolution XPS spectra of (c) Pb 4f and (d) I 3d peaks, (e) XRD patterns, and (f) absorbance spectra of the $MAPbI_3$ and $MAPbI_3$/xGQDs ($x = 0.001$, 0.005, and 0.01) perovskite films.

PbI_2 residues usually exist in the perovskite films obtained from the two-step deposition process [21]. However, the $MAPbI_3$/0.001GQDs perovskite film does not show any PbI_2 residue, indicating that appropriate GQDs are beneficial for the reaction between the PbI_2 and MAI, and then resulting in the best $MAPbI_3$ film with the purest phase structure. Following, the crystallite sizes of the $MAPbI_3$ and $MAPbI_3$/xGQDs (x = 0.001, 0.005, and 0.01) perovskite films were evaluated by the Scherrer formula based on their full width at half maximums of (110) peaks. The $MAPbI_3$ film exhibits the crystallite size of about 58.6 nm, whereas the crystallite size of the $MAPbI_3$/0.001GQDs film is determined to be 60.62 nm. This result indicates that the incorporation of the GQDs into the $MAPbI_3$ precursor solution will also beneficial for the crystal growth. Figure 2(f) shows the UV–Vis absorption spectra of the $MAPbI_3$ and $MAPbI_3$/xGQDs (x = 0.001, 0.005, and 0.01) perovskite films. Clearly, the four kinds of films exhibit similar absorption edge at around 785 nm, indicating the bandgap of $MAPbI_3$ perovskite (about 1.58 eV) will not be affected by the incorporation of the GQDs. Intriguingly, the $MAPbI_3$/0.001GQDs perovskite film has a slightly enhanced absorbance in the visible light range, which can be attributed to its relatively purer phase structure and larger crystallite size.

In order to investigate the effects of GQDs on the morphology of the $MAPbI_3$ perovskite films, scanning electron microscope (SEM) images of the $MAPbI_3$ and $MAPbI_3$/xGQDs (x = 0.001, 0.005, and 0.01) perovskite films were characterized, as shown in figure 3. The left column in figure 3 illustrates the top-view SEM images of the four samples. Clearly, the morphologies of the four samples are very alike, which are uniform, dense-packed, and without any pinholes. Despite the GQDs cannot be observed by SEM, we consider that the GQDs mainly locate at the grain boundaries of perovskites. In order to find the GQDs at the grain boundaries, we tried to increase the concentration of the GQDs to 0.1 mg ml^{-1} [45], however, it is still difficult for us to distinguish the GQDs from the perovskite grains boundaries (figure S3), which can be ascribed to the still low concentration of the GQD, the small size of the GQD, and a good dispersity of the GQD in the whole film. In theory, because the bonding between the GQDs and PbI_2 is weaker than that between MAI and PbI_2, the GQDs will be repelled during the formation process of $MAPbI_3$ [32]. Thus, we speculated that the GQDs finally aggregate at the grain boundaries when the perovskite grain growth is completed. The statistical average grain size of the $MAPbI_3$/0.001GQDs perovskite film is around 580 nm, which is larger than that of the $MAPbI_3$, $MAPbI_3$/0.005GQDs, and $MAPbI_3$/0.01GQDs perovskite films (570, 520, and 510 nm). Such difference of the grain sizes could be attributed to the following two reasons. On one hand, the lone unpaired electrons of carbonyl (−C=O) and carboxylic (–COOH) on GQDs may interact with PbI_2 and thus decelerate the crystallization rate [46, 47]. On the other hand, the existent of the trace water in the GQDs solution would prompt the crystallization and improve the surface coverage [48–50]. Additionally, the right column in figure 3 displays the cross-sectional SEM images of PSCs based on the four kinds of perovskite films, which demonstrate the electron transport layers of the mesoporous TiO_2 and the hole transport layers of the spiro-OMeTAD contact with the perovskite layers smoothly. Obviously, the $MAPbI_3$/0.001GQDs perovskite layer in figure 3(d) grows perpendicular to the substrate and almost no horizontal grain boundaries can be found, which will be beneficial for the carrier transport. In short, all of the results obtained from figure 3 imply that the $MAPbI_3$/0.001GQDs perovskite film shows the best morphology for the applications in PSCs among the four kinds of perovskite films.

To investigate the distribution of the GQDs in the $MAPbI_3$/xGQDs (x = 0.001, 0.005, and 0.01) perovskite films, fluorescence images were captured using a confocal laser scanning microscope. The $MAPbI_3$/0.01GQDs perovskite film was chose to test here because of its high concentration of the GQDs. The optical profile of this perovskite is clearly observed from the bright field image (figure 4(a)), which shows the same surface morphology with that in figure 3(g). The collected emissions from GQDs were set in the range of 500 nm to 580 nm to avoid the disturbance caused by PbI_2, as shown the green dots in figure 4(b). It can be found that the GQDs are distributed homogeneously in the $MAPbI_3$/0.01GQDs film, which suggests that the charge diffusion will be uniform and smooth in the $MAPbI_3$/xGQDs (x = 0.001, 0.005, and 0.01) perovskite films.

The steady-state (PL spectra of the $MAPbI_3$ and $MAPbI_3$/xGQDs (x = 0.001, 0.005, and 0.01) perovskite films on glass substrates were measured, as shown in figure 4(d). Clearly, the emission peaks for the four samples are at around 772 nm, indicating that the incorporation of GQDs does not affect the bandgap of the $MAPbI_3$ perovskite film, which is in accordance with the results obtained from figure 2(f). Moreover, the PL intensity of the $MAPbI_3$/xGQDs (x = 0.001, 0.005, and 0.01) perovskite film is much stronger than that of the $MAPbI_3$ perovskite films, and $MAPbI_3$/0.001GQDs perovskite film shows the strongest PL intensity among them. It is well known that the steady-state PL intensity depends on the recombination of photo-induced charge carriers [51]. Therefore, the stronger PL intensity indicates lower electron–hole recombination rate and lower trap states in the $MAPbI_3$/xGQDs perovskite films. To further gain more insight into the effects of the GQDs on the carrier lifetime of the $MAPbI_3$ perovskite film, time–resolved PL spectra were performed, as shown in figure 4(e). A bi-exponential decay function was used to fit the PL decay time of the samples. Generally, the fast decay lifetime τ_1 is ascribed to non-radiative trap assisted recombination and the slow decay lifetime τ_2 is assigned as exciton recombination [52, 53]. For the $MAPbI_3$ perovskite film, the PL decay lifetime of τ_1 and τ_2 are 3.3 ns and 100.1 ns, respectively, while they are increased to 4.3 ns and 460.5 ns, respectively, for the $MAPbI_3$/0.001GQDs perovskite film. Such enhanced lifetime further demonstrates that the GQDs reduce the defect states effectively in the $MAPbI_3$/0.001GQDs perovskite film [54].

Figure 5(a) shows the current density–voltage (J–V) curves of the PSCs based on the $MAPbI_3$ and $MAPbI_3$/xGQDs (x = 0.001, 0.005, and 0.01) perovskite films. The corresponding photovoltaic parameters are listed in table 1. As a control sample, the PSC based on the $MAPbI_3$ film shows

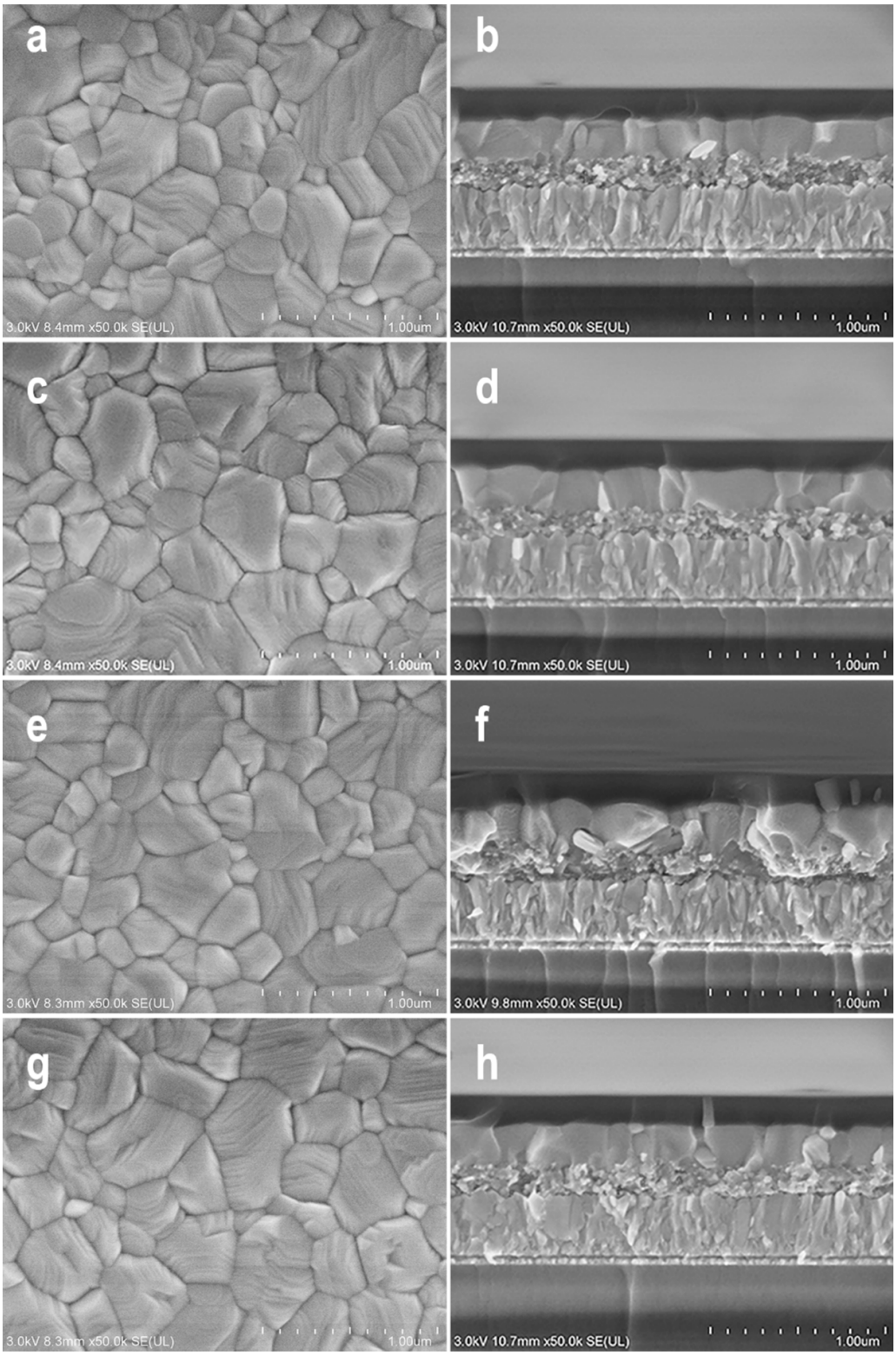

Figure 3. Top-view SEM images of the (a) $MAPbI_3$, (c) $MAPbI_3$/0.001GQDs, (e) $MAPbI_3$/0.005GQDs, and (g) $MAPbI_3$/0.01GQDs perovskite films. Cross-sectional SEM images of the PSCs based on the (b) $MAPbI_3$, (d) $MAPbI_3$/0.001GQDs, (f) $MAPbI_3$/0.005GQDs, and (h) $MAPbI_3$/0.01GQDs perovskite films.

an open-circuit voltage (V_{OC}) of 1.072 V, a short-circuit current density (J_{SC}) of 22.25 mA cm^{-2}, a fill factor (FF) of 67.3%, and a PCE of 16.05%. After incorporating the GQDs into the $MAPbI_3$ films, the PSCs based on the $MAPbI_3$/xGQDs (x = 0.001, 0.005, and 0.01) films display clear increases in all parameters. Particularly, the PSC based on the $MAPbI_3$/0.001GQDs film exhibits the highest PCE of 19.59% with a J_{SC} of 23.36 mA cm^{-2}, a V_{OC} of 1.158 V,

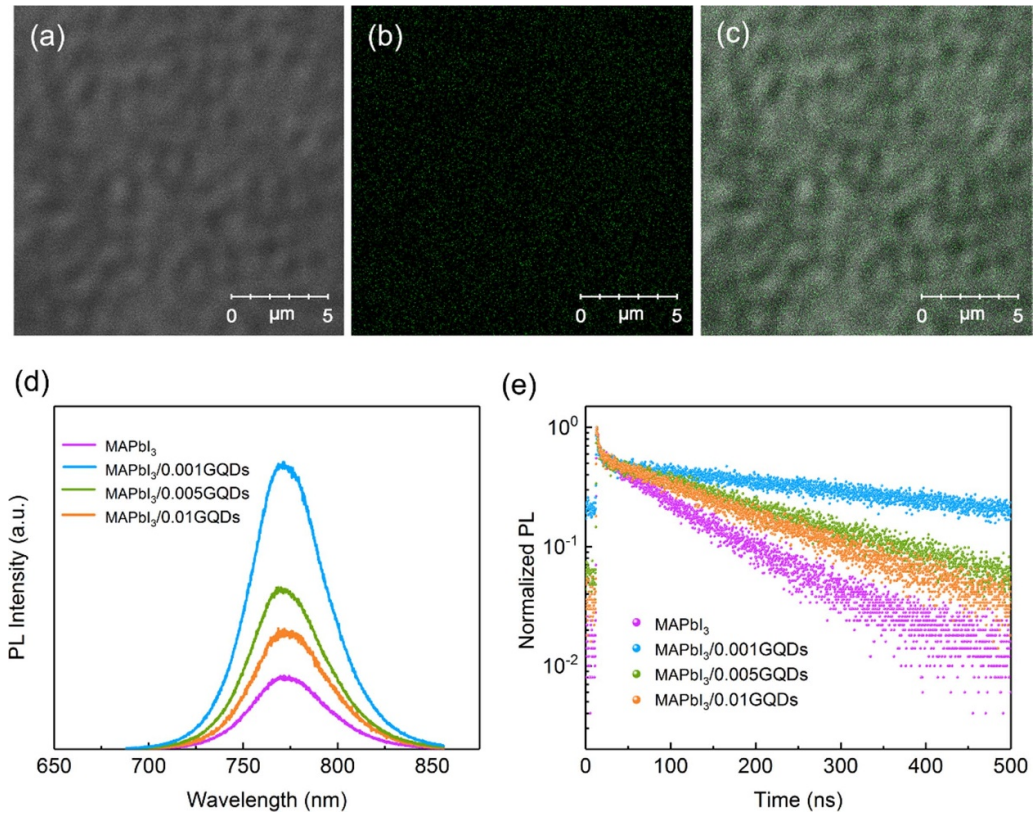

Figure 4. CLSM images of the $MAPbI_3$/0.01GQDs perovskite films: (a) bright field image, (b) fluorescence image and (c) merged image. (d) Steady-state PL and (e) TRPL spectra of the $MAPbI_3$ and $MAPbI_3$/*x*GQDs ($x = 0.001$, 0.005, and 0.01) perovskite films on glass substrates, respectively.

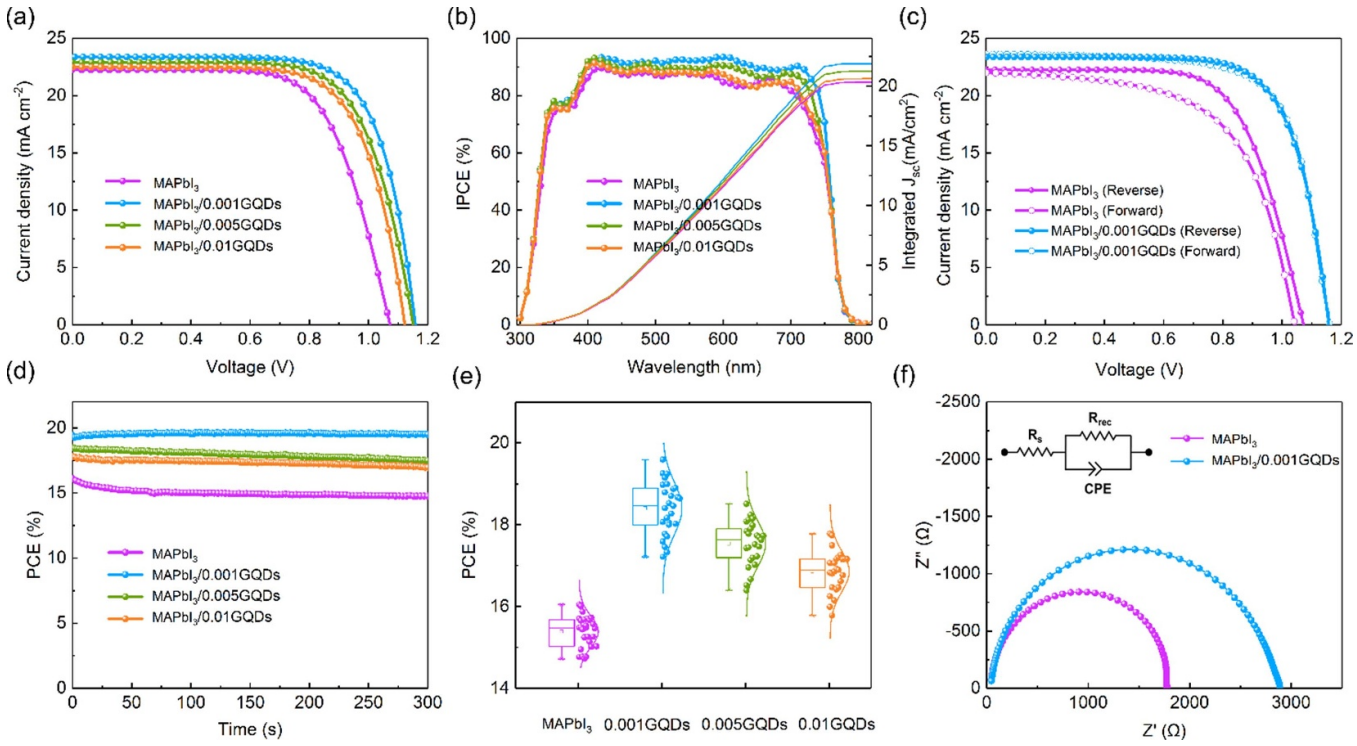

Figure 5. (a) *J*–*V* curves and (b) IPCE spectra and integrated J_{SC} of the PSCs based on the $MAPbI_3$ and $MAPbI_3$/*x*GQDs ($x = 0.001$, 0.005, and 0.01) perovskite films, respectively. (c) *J*–*V* curves of the PSCs based on the $MAPbI_3$ and $MAPbI_3$/0.001GQDs perovskite films under reverse and forward scan modes, respectively. (d) Steady-state output PCEs at the maximum power point. (e) Box statistical diagram of the PCEs. (f) Nyquist plots of the PSCs based on the $MAPbI_3$ and $MAPbI_3$/0.001GQDs perovskite films, respectively. The inset displays the equivalent circuit.

Table 1. Photovoltaic parameters of the PSCs based on the $MAPbI_3$ and $MAPbI_3$/*x*GQDs ($x = 0.001$, 0.005, and 0.01) perovskite films.

Sample		V_{oc} (V)	J_{sc} (mA cm^{-2})	FF (%)	PCE (%)
$MAPbI_3$	Best	1.072	22.25	67.3	16.05
	Average	1.073 ± 0.003	21.72 ± 0.26	66.0 ± 1.3	15.39 ± 0.38
$MAPbI_3$/0.001GQDs	Best	1.158	23.36	72.4	19.59
	Average	1.153 ± 0.004	22.96 ± 0.64	69.5 ± 1.0	18.40 ± 0.64
$MAPbI_3$/0.005GQDs	Best	1.150	22.90	70.3	18.51
	Average	1.149 ± 0.006	22.37 ± 0.62	68.2 ± 1.1	17.54 ± 0.55
$MAPbI_3$/0.01GQDs	Best	1.122	22.49	70.4	17.78
	Average	1.132 ± 0.006	22.10 ± 0.50	67.4 ± 1.1	16.86 ± 0.51

and a FF of 72.4%, respectively. Moreover, a smaller concentration of 0.0005 mg ml^{-1} GQDs was also investigated, but the obtained PCE of 18.28% and FF of 71% were still lower than those of PSCs based on the $MAPbI_3$/0.001GQDs films (figure S4 and table S1). Compared with the control sample, such large increases in the PSC based on the $MAPbI_3$/0.001GQDs film can be ascribed to the pure phase structure, high-quality morphology, low defect density, and high electrical conductivity caused by the incorporation of the GQDs. Figure 5(b) shows the incident photon-to-charge conversion efficiency (IPCE) spectra of the four PSCs. Obviously, the PSC based on the $MAPbI_3$/0.001GQDs film shows an obvious enhanced IPCE in the entire wavelength region, especially in the wavelength range from 600 to 800 nm. The improved response in the long wavelength range means that the photo-electrons in the deeper region of the perovskite film could be collected more effectively after incorporating GQDs, which further confirms that GQDs interact with perovskite and form a bulk heterojunction [34]. The integrated J_{SC} calculated from IPCE is also displayed in figure 5(b), which is close to the *J*–*V* scan results.

The anomalous hysteresis effects usually exist in PSCs when they are tested under forward and reverse scan modes, which can be attributed to the ion migrations, ferroelectric polarizations and trap states in perovskites and interfaces [55, 56]. Figure 5(c) shows the *J*–*V* curves of the PSCs based on the $MAPbI_3$ and $MAPbI_3$/0.001GQDs films under the forward and reverse scan modes, respectively. The PSC based on the $MAPbI_3$ film displays a very large hysteresis, while the PSC based on the $MAPbI_3$/0.001GQDs film reveals almost negligible hysteresis. The hysteresis indexes (HIs) of the two kinds of PSCs can be calculated by the equation of $(PCE_{reverse} - PCE_{forward})/PCE_{reverse}$, where the $PCE_{reverse}$ and $PCE_{forward}$ represent the PCEs tested under the reverse and forward scan modes, respectively. As a result, the HIs for the PSCs based on the $MAPbI_3$ and $MAPbI_3$/0.001GQDs films were calculated to be 0.133 and 0.007 respectively. The decreased HI can be ascribed to the low defect density and low MA^+/I^- migration because of the introduction of the GQDs according to previous reports [57]. The steady-state output PCEs were measured to confirm the operation status of PSCs. As shown in figure 5(d), the $MAPbI_3$/0.001GQDs PSC maintains a stabilized output PCE of 19.5% at the maximum power point ($V_{MPP} = 0.922$ V), which is consistent with that attained from reverse scan. In contrast, the $MAPbI_3$ PSC shows a declined PCE of 14.7% at the $V_{MPP} = 0.797$ V. The statistical distribution of the PCEs based on 25 devices for each kind of PSCs is shown in figure 5(e). The $MAPbI_3$/*x*GQDs PSCs show apparently enhanced PCE as compared with the $MAPbI_3$ PSCs. Electrochemical impedance spectroscopy (EIS) was conducted to further study the effects of the GQDs on the charge transport and recombination behaviors in the $MAPbI_3$ films [58, 59]. Figure 5(f) shows the Nyquist plots of the PSCs based on the $MAPbI_3$ and $MAPbI_3$/0.001GQDs films in the dark condition with a bias voltage of 0.9 V, where the inset image is the equivalent circuit. The primary arc reflects the charge recombination (R_{rec}) process within the PSCs. The PSC based on the $MAPbI_3$/0.001GQDs film exhibits a much larger R_{rec} than the PSC based on the $MAPbI_3$ film (2888 *vs*. 1772 Ω), which indicates the charge recombination in the PSC based on the $MAPbI_3$/0.001GQDs film was effectively diminished due to the low defect density caused by the incorporation of the GQDs.

According to the above analyses, a credible mechanism of the $MAPbI_3$ perovskites with the GQDs is depicted in figure 6. It is well known that there are many kinds of defects in the $MAPbI_3$ perovskites, like Pb vacancies, I vacancies, and so on, all of which will lead to severe carrier recombination [60, 61]. Such severe recombination will decrease the carrier extraction efficiency, and then lead to lower current and voltage. We suppose that these disadvantages will be weakened after the incorporation of the GQDs in this work. Figure 6(d) shows that the functional groups in GQDs, like carbonyl and carboxylic, could coordinate with the unsaturated Pb^{2+} ions in the $MAPbI_3$ perovskites, which will reduce the defect density and then inhibit the charge recombination effectively. Meanwhile, the hydroxyl functional groups in GQDs would link with I^- ions in the $MAPbI_3$ perovskites via hydrogen bonding, which will inhibit ion migrations and then increase the structure stability of the frameworks. Besides, the single-crystalline GQDs possess good conductivities, therefore, the incorporation of GQDs will improve the electrical conductivity of the $MAPbI_3$/*x*GQDs ($x = 0.001$, 0.005, and 0.01) films, which is beneficial for the carrier transport in them, as shown in figures 6(b) and (c). The last but not the least, because the conduction band minimum (CBM) of the GQDs is relatively higher than TiO_2 electron transport layer (ETL) [62], gradient energy levels are formed in the PSCs based on the $MAPbI_3$/*x*GQDs ($x = 0.001$, 0.005, and 0.01) films, which will lead to a high-speed electron transport from the CBM of the perovskite layer to that of the TiO_2 layer, as shown in figure S5.

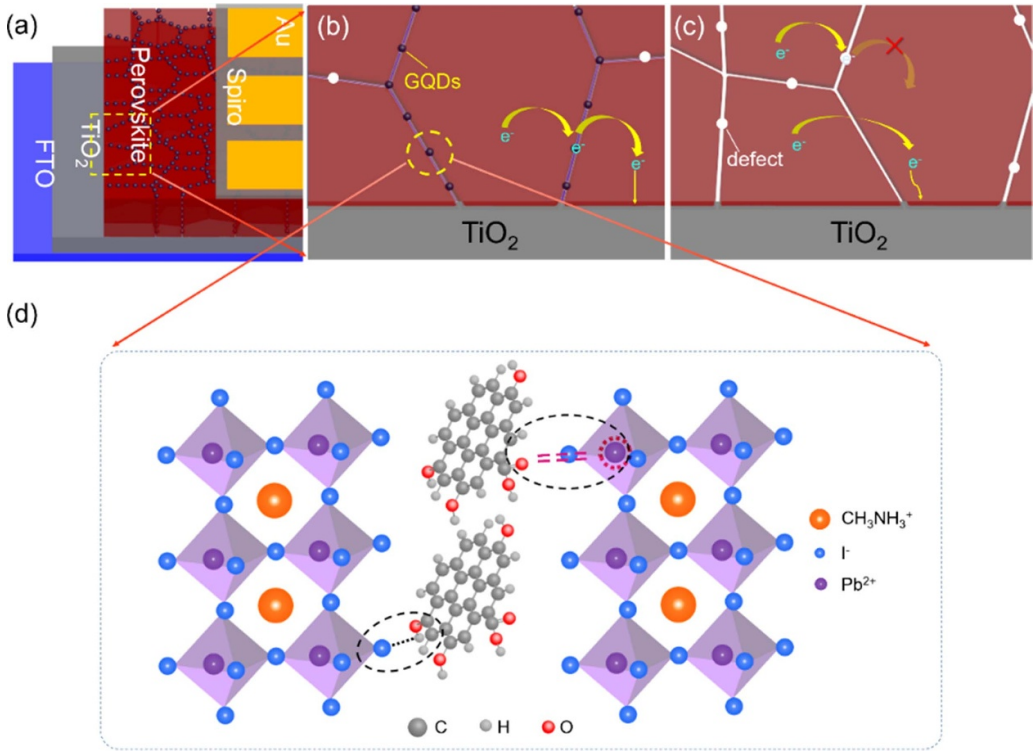

Figure 6. (a) Schematic diagram of the PSC based on the $MAPbI_3$/0.001GQDs film. Schematic diagrams of the charge transport in the (b) $MAPbI_3$ and (c) $MAPbI_3$/0.001GQDs perovskite films. (d) Crystal structure of the $MAPbI_3$/0.001GQDs perovskite.

To investigate the trap densities and hole mobilities of the $MAPbI_3$ and $MAPbI_3$/xGQDs (x = 0.001, 0.005, and 0.01) perovskite films experimentally, the hole-only devices with the structure of FTO/PEDOT:PSS/perovskite/spiro-OMeTAD/Au were fabricated. As shown in figure 7(a), three regions can be identified at different voltage range: ohmic region, trap-filled limited (TFL) region, and space-charge-limited current (SCLC) region. The linear relationship at the low bias voltage represents the ohmic response of the PSCs. When the voltage exceeds the kink point (V_{TFL}), the current nonlinearly increases, indicating that the trap states are completely filled. The trap density (n_t) can be calculated by the following formula: $V_{\mathrm{TFL}} = en_t d^2/2\varepsilon_0\varepsilon$, where e is the elementary charge, d is the thickness of the film, ε is the relative permittivity of $MAPbI_3$ (ε = 32), ε_0 is the vacuum dielectric constant, and V_{TFL} is the trap-filled limit voltage [63]. As shown in table S2, compared with the $MAPbI_3$ perovskite (1.57×10^{16} cm^{-3}), the trap density of the $MAPbI_3$/0.001GQDs perovskite is reduced to be 7.08×10^{15} cm^{-3}, which confirms our supposition in figure 6 that the incorporation of the GQDs will reduce the trap density in the $MAPbI_3$ perovskite. Moreover, the mobility (μ) of the various perovskite films can also be calculated by the Mott–Gurney law in the SCLC region by the following formula: $J = 9\varepsilon\varepsilon_0\mu V_b{}^2/8d^3$, where J is the current density, and V_b is the applied voltage [64]. The hole mobilities of the $MAPbI_3$ and $MAPbI_3$/xGQDs (x = 0.001, 0.005, and 0.01) perovskite films derived from figure 7(b) are also summarized in table S2. The mobility of $MAPbI_3$/0.001GQDs perovskite is 8.56×10^{-3} cm^2 V^{-1} s^{-1}, which is much larger than the $MAPbI_3$ perovskite (3.84×10^{-3} cm^2 V^{-1} s^{-1}). The improved charge mobility is a main reason for the enhanced photovoltaic performance as well.

The water contact angles of the perovskite films were measured to evaluate the hydrophilic performances of the $MAPbI_3$ and $MAPbI_3$/xGQDs (x = 0.001, 0.005, and 0.01) perovskite films, as shown in figure S6. The contact angles of the $MAPbI_3$/xGQDs (x = 0.001, 0.005, and 0.01) perovskite films have slight increases when compared with that of the $MAPbI_3$ film, which can be ascribed to the hydrophobic characteristic of graphene. It is well known that the contact angle evolution could reflect the decomposition of perovskite films when they are exposed to the water droplets. Therefore, the incorporation of GQDs in the $MAPbI_3$ perovskite will provide better water-repellent property for the $MAPbI_3$/xGQDs (x = 0.001, 0.005, and 0.01) perovskite films. In order to study the thermal stabilities of the $MAPbI_3$ and $MAPbI_3$/xGQDs (x = 0.001, 0.005, and 0.01) perovskite films, the thermogravimetric analyses were performed on the four samples in the argon atmosphere, as shown in figure 7(c). There are two main steps of the weight loss at 200 °C–300 °C and 450 °C–550 °C, which are correlated with the sublimation of MAI and PbI_2 respectively [65]. For the $MAPbI_3$ perovskite, the weight loss starts at around 195 °C, while the temperature gradually increases to 230 °C in the $MAPbI_3$/xGQDs (x = 0.001, 0.005, and 0.01) perovskites, which suggests that the thermal stability of the $MAPbI_3$ perovskite is improved dramatically after incorporating the GQDs. Finally, the environmental stability of the unsealed devices was also tested in the ambient

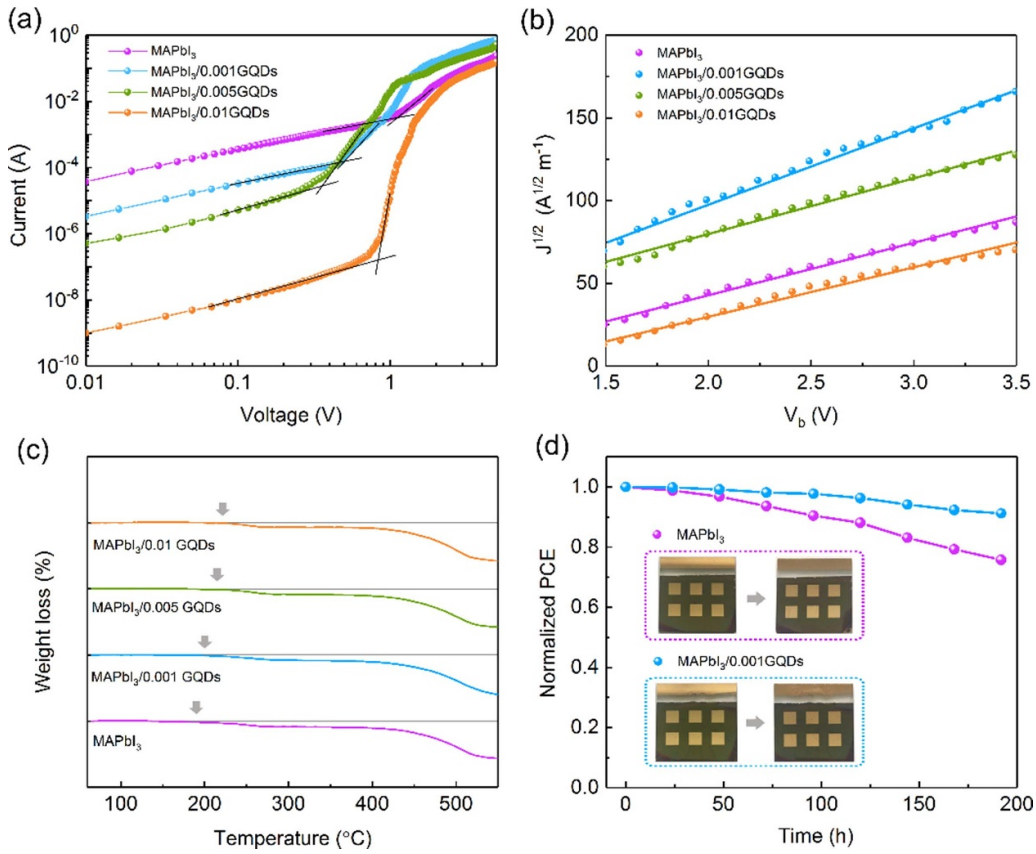

Figure 7. (a) Dark current–voltage curves of the hole-only devices with the structure of FTO/PEDOT:PSS/perovskite/spiro-OMeTAD/Au. The perovskite layers are the $MAPbI_3$ and $MAPbI_3$/*x*GQDs ($x = 0.001$, 0.005, and 0.01) perovskite films respectively. (b) Hole mobility measurement using the SCLC model. (c) TGA curves of the $MAPbI_3$ and $MAPbI_3$/*x*GQDs ($x = 0.001$, 0.005, and 0.01) perovskite films. (d) Stability of the unsealed PSCs based on the $MAPbI_3$ and $MAPbI_3$/0.001GQDs films in the ambient atmosphere with a humidity of 35%–45%. The inset photographs are the corresponding initial and 200 h-stored PSCs.

atmosphere with a humidity of 35%–45%. Figure 7(d) shows the normalized PCE decays versus the storage time of the PSCs based on the $MAPbI_3$ and $MAPbI_3$/0.001GQDs perovskite films, respectively. Remarkably, the PSC based on the $MAPbI_3$/0.001GQDs perovskite film retains 91.2% of its initial PCE after around 200 h, while the PSC based on the $MAPbI_3$ film retains only 75.8% of its initial PCE, indicating the incorporation of the GQDs can improve the stability of the $MAPbI_3$ perovskites in air effectively.

4. Conclusion

In summary, the $MAPbI_3$/0.001GQDs composite film was successfully prepared by a dynamic two-step spin-coating process. After incorporating the GQDs into the $MAPbI_3$, this perovskite exhibited a pure phase structure and high-quality morphology, which provided a smooth path for the charge transport in the $MAPbI_3$/0.001GQDs perovskite film. More importantly, the $MAPbI_3$/0.001GQDs perovskite film also displayed low trap density and high electrical conductivity, improving the carrier separation and transport ability, prolonging the carrier lifetime and reducing the nonradiative recombination rate. As a result, the PSCs based on the $MAPbI_3$/0.001GQDs films showed a dramatically enhanced PCE compared to the PSCs based on the bare $MAPbI_3$ films. Moreover, the new PSCs were demonstrated to have good long-term stability and resistibility against heat and moisture. This study not only reveals the underlying factors contributing to the perovskite research community, but also opens the door for further exploring novel approaches to enhance the quality of perovskite films.

Acknowledgments

This work was supported by the National Natural Science Foundation of China (Nos. 52202178, 21901154, and 52102219), the Natural Science Foundation of Shanghai (Nos. 22ZR1426300 and 21ZR1404900), the Shanghai Sailing Program (No. 19YF1417600), and the Shanghai Pujiang Project (No. 21PJ1400900). The authors declare no competing financial interest.

ORCID iD

Jia Liang https://orcid.org/0000-0002-4352-1581

References

[1] Stranks S D, Eperon G E, Grancini G, Menelaou C, Alcocer M J P, Leijtens T, Herz L M, Petrozza A and Snaith H J 2013 Electron-hole diffusion lengths exceeding 1 micrometer in an organometal trihalide perovskite absorber *Science* **342** 341

[2] Jena A K, Kulkarni A and Miyasaka T 2019 Halide perovskite photovoltaics: background, status, and future prospects *Chem. Rev.* **119** 3036

[3] Jiang Q, Zhao Y, Zhang X W, Yang X L, Chen Y, Chu Z M, Ye Q F, Li X X, Yin Z G and You J B 2019 Surface passivation of perovskite film for efficient solar cells *Nat. Photon.* **13** 460

[4] Chen H *et al* 2017 A solvent- and vacuum-free route to large-area perovskite films for efficient solar modules *Nature* **550** 92

[5] Saliba M *et al* 2016 Cesium-containing triple cation perovskite solar cells: improved stability, reproducibility and high efficiency *Energy Environ. Sci.* **9** 1989

[6] Han X, Xiong H, Qi J, Rui Y, Zhang X, Hou C, Li Y, Wang H and Zhang Q 2019 Controlling the transformation of intermediate phase under near-room temperature for improving the performance of perovskite solar cells *Sol. Energy* **186** 225

[7] Li T P, Rui Y C, Wang X J, Shi J S, Wang Y Q, Yang J X and Zhang Q H 2021 Grain size and interface modification via cesium carbonate post-treatment for efficient SnO_2-based planar perovskite solar cells *ACS Appl. Energy Mater.* **4** 7002

[8] Wang X, Zhao Y, Li B, Han X, Jin Z, Wang Y, Zhang Q and Rui Y 2022 Interfacial modification via a 1,4-butanediamine-based 2D capping layer for perovskite solar cells with enhanced stability and efficiency *ACS Appl. Mater. Interfaces* **14** 22879

[9] Chen Q, Zhou H P, Hong Z R, Luo S, Duan H S, Wang H H, Liu Y S, Li G and Yang Y 2014 Planar heterojunction perovskite solar cells via vapor-assisted solution process *J. Am. Chem. Soc.* **136** 622

[10] Jung M, Ji S G, Kim G and Seok S I 2019 Perovskite precursor solution chemistry: from fundamentals to photovoltaic applications *Chem. Soc. Rev.* **48** 2011

[11] Zhao P J, Kim B J and Jung H S 2018 Passivation in perovskite solar cells: a review *Mater. Today Energy* **7** 267

[12] Wang Y B, Wu T H, Barbaud J, Kong W Y, Cui D Y, Chen H, Yang X D and Han L Y 2019 Stabilizing heterostructures of soft perovskite semiconductors *Science* **365** 687

[13] Alberti A, Bongiorno C, Smecca E, Deretzis I, La Magna A and Spinella C 2019 Pb clustering and PbI_2 nanofragmentation during methylammonium lead iodide perovskite degradation *Nat. Commun.* **10** 2196

[14] Shi J, Li B, Zhang Q and Rui Y 2021 Electrodeposited ternary $AgCuO_2$ nanocrystalline films as hole transport layers for inverted perovskite solar cells *J. Alloys Compd.* **890** 161879

[15] Jiang Y, Juarez-Perez E J, Ge Q, Wang S, Leyden M R, Ono L K, Raga S R, Hu J and Qi Y 2016 Post-annealing of $MAPbI_3$ perovskite films with methylamine for efficient perovskite solar cells *Mater. Horiz.* **3** 548

[16] Jiang Y, Yang S-C, Jeangros Q, Pisoni S, Moser T, Buecheler S, Tiwari A N and Fu F 2020 Mitigation of vacuum and illumination-induced degradation in perovskite solar cells by structure engineering *Joule* **4** 1087

[17] Chen B, Rudd P N, Yang S, Yuan Y B and Huang J S 2019 Imperfections and their passivation in halide perovskite solar cells *Chem. Soc. Rev.* **48** 3842

[18] Yang J, Liu C, Cai C S, Hu X T, Huang Z Q, Duan X P, Meng X C, Yuan Z Y, Tan L C and Chen Y W 2019 High-performance perovskite solar cells with excellent humidity and thermo-stability via fluorinated perylenediimide *Adv. Energy Mater.* **9** 1900198

[19] Ono L K, Liu S Z and Qi Y B 2020 Reducing detrimental defects for high-performance metal halide perovskite solar cells *Angew. Chem., Int. Ed.* **59** 6676

[20] Li H, Wu G H, Li W Y, Zhang Y H, Liu Z K, Wang D P and Liu S Z 2019 Additive engineering to grow micron-sized grains for stable high efficiency perovskite solar cells *Adv. Sci.* **6** 190124

[21] Son D Y *et al* 2016 Self-formed grain boundary healing layer for highly efficient $CH_3NH_3PbI_3$ perovskite solar cells *Nat. Energy* **1** 16081

[22] Jiang Q, Chu Z N, Wang P Y, Yang X L, Liu H, Wang Y, Yin Z G, Wu J L, Zhang X W and You J B 2017 Planar-structure perovskite solar cells with efficiency beyond 21% *Adv. Mater.* **29** 1703852

[23] Niu T Q *et al* 2018 Stable high-performance perovskite solar cells via grain boundary passivation *Adv. Mater.* **30** 1706576

[24] Wang R *et al* 2019 Caffeine improves the performance and thermal stability of perovskite solar cells *Joule* **3** 1464

[25] Bi D Q *et al* 2018 Multifunctional molecular modulators for perovskite solar cells with over 20% efficiency and high operational stability *Nat. Commun.* **9** 4482

[26] Ali J *et al* 2020 Interfacial and structural modifications in perovskite solar cells *Nanoscale* **12** 5719

[27] Chen W *et al* 2019 Conjugated polymer-assisted grain boundary passivation for efficient inverted planar perovskite solar cells *Adv. Funct. Mater.* **29** 1808855

[28] Peng J *et al* 2012 Graphene quantum dots derived from carbon fibers *Nano Lett.* **12** 844

[29] Zhang S, Sui L N, Dong H Z, He W B, Dong L F and Yu L Y 2018 High-performance supercapacitor of graphene quantum dots with uniform sizes *ACS Appl. Mater. Interfaces* **10** 12983

[30] Wang L, Li W T, Li M, Su Q Q, Li Z, Pan D Y and Wu M H 2018 Ultrastable amine, sulfo cofunctionalized graphene quantum dots with high two-photon fluorescence for cellular imaging *ACS Sustain. Chem. Eng.* **6** 4711

[31] Wang L *et al* 2020 Full-color fluorescent carbon quantum dots *Sci. Adv.* **6** eabb6772

[32] Ma Y H *et al* 2019 Enhancing the performance of inverted perovskite solar cells via grain boundary passivation with carbon quantum dots *ACS Appl. Mater. Interfaces* **11** 3044

[33] Hsu H L, Hsiao H T, Juang T Y, Jiang B H, Chen S C, Jeng R J and Chen C P 2018 Carbon nanodot additives realize high-performance air-stable p-i-n perovskite solar cells providing efficiencies of up to 20.2% *Adv. Energy Mater.* **8** 1802323

[34] Li H *et al* 2018 Graphdiyne-based bulk heterojunction for efficient and moisture-stable planar perovskite solar cells *Adv. Energy Mater.* **8** 1802012

[35] Liu K, Chen S, Wu J, Zhang H, Qin M, Lu X, Tu Y, Meng Q and Zhan X 2018 Fullerene derivative anchored SnO_2 for high-performance perovskite solar cells *Energy Environ. Sci.* **11** 3463

[36] Wang L *et al* 2014 Gram-scale synthesis of single-crystalline graphene quantum dots with superior optical properties *Nat. Commun.* **5** 5357

[37] Rui Y, Li T, Li B, Wang Y and Müller-Buschbaum P 2022 Two-dimensional SnS_2 nanosheets as electron transport and interfacial layers enable efficient perovskite solar cells *J. Mater. Chem.* C **10** 12392–401

[38] Zhang X, Rui Y, Yang J, Wang L, Wang Y and Xu J 2019 Monodispersed SnO_2 microspheres aggregated by tunable building units as effective photoelectrodes in solar cells *Appl. Surf. Sci.* **463** 679

[39] Fan X Y, Rui Y C, Han X F, Yang J X, Wang Y Q and Zhang Q H 2020 Spray-coated monodispersed SnO_2

microsphere films as scaffold layers for efficient mesoscopic perovskite solar cells *J. Power Sources* **448** 227405
[40] Xu Q F, Zhou Q, Hua Z, Xue Q, Zhang C F, Wang X Y, Pan D Y and Xiao M 2013 Single-particle spectroscopic measurements of fluorescent graphene quantum dots *ACS Nano* **7** 10654
[41] Liu W W, Feng Y Q, Yan X B, Chen J T and Xue Q J 2013 Superior micro-supercapacitors based on graphene quantum dots *Adv. Funct. Mater.* **23** 4111
[42] Wang Y, Zhou Y Y, Zhang T Y, Ju M-G, Zhang L, Kan M, Li Y H, Zeng X C, Padture N P and Zhao Y X 2018 Integration of a functionalized graphene nano-network into a planar perovskite absorber for high-efficiency large-area solar cells *Mater. Horiz.* **5** 868
[43] Xu G Q *et al* 2020 Low optical dosage heating-reduced viscosity for fast and large-scale cleanup of spilled crude oil by reduced graphene oxide melamine nanocomposite adsorbents *Nanotechnology* **31** 225402
[44] Lee J W, Bae S H, Hsieh Y T, De Marco N, Wang M K, Sun P Y and Yang Y 2017 A bifunctional lewis base additive for microscopic homogeneity in perovskite solar cells *Chem* **3** 290
[45] Zhang W, Xiong J, Li J and Daoud W A 2021 Organic dye passivation for high-performance all-inorganic $CsPbI_{1.5}Br_{1.5}$ perovskite solar cells with efficiency over 14% *Adv. Energy Mater.* **11** 2003585
[46] Zheng X P *et al* 2018 Dual functions of crystallization control and defect passivation enabled by sulfonic zwitterions for stable and efficient perovskite solar cells *Adv. Mater.* **30** 1803428
[47] Lee J W, Kim H S and Park N G 2016 Lewis acid-base adduct approach for high efficiency perovskite solar cells *Acc. Chem. Res.* **49** 311
[48] Gong X, Li M, Shi X B, Ma H, Wang Z K and Liao L S 2015 Controllable perovskite crystallization by water additive for high-performance solar cells *Adv. Funct. Mater.* **25** 6671
[49] Deng Y H, Peng E, Shao Y C, Xiao Z G, Dong Q F and Huang J S 2015 Scalable fabrication of efficient organolead trihalide perovskite solar cells with doctor-bladed active layers *Energy Environ. Sci.* **8** 1544
[50] He T W, Liu Z Y, Zhou Y and Ma H 2018 The stable perovskite solar cell prepared by rapidly annealing perovskite film with water additive in ambient air *Sol. Energy Mater. Sol. Cells* **176** 280
[51] Li T, Rui Y, Zhang X, Shi J, Wang X, Wang Y, Yang J and Zhang Q 2020 Anatase TiO_2 nanorod arrays as high-performance electron transport layers for perovskite solar cells *J. Alloys Compd.* **849** 156629
[52] Zheng X P, Chen B, Dai J, Fang Y J, Bai Y, Lin Y Z, Wei H T, Zeng X C and Huang J S 2017 Defect passivation in hybrid perovskite solar cells using quaternary ammonium halide anions and cations *Nat. Energy* **2** 17102
[53] Mali S S, Shim C S, Kim H and Hong C K 2016 Reduced graphene oxide (RGO) grafted zinc stannate (Zn_2SnO_4) nanofiber scaffolds for highly efficient mixed-halide perovskite solar cells *J. Mater. Chem.* A **4** 12158
[54] Zhang X, Rui Y, Wang Y, Xu J, Wang H, Zhang Q and Müller-Buschbaum P 2018 SnO_2 nanorod arrays with tailored area density as efficient electron transport layers for perovskite solar cells *J. Power Sources* **402** 460
[55] Snaith H J, Abate A, Ball J M, Eperon G E, Leijtens T, Noel N K, Stranks S D, Wang J T W, Wojciechowski K and Zhang W 2014 Anomalous hysteresis in perovskite solar cells *J. Phys. Chem. Lett.* **5** 1511
[56] Zheng X L, Wei Z H, Chen H N, Zhang Q P, He H X, Xiao S, Fan Z Y, Wong K S and Yang S H 2016 Designing nanobowl arrays of mesoporous TiO_2 as an alternative electron transporting layer for carbon cathode-based perovskite solar cells *Nanoscale* **8** 6393
[57] Ogunniran K O, Murugadoss G, Thangamuthu R, Karthikeyan J and Murugan P 2019 Integration of phenylammoniumiodide (PAI) as a surface coating molecule towards ambient stable $MAPbI_3$ perovskite for solar cell application *Sol. Energy Mater. Sol. Cells* **191** 316
[58] Mahmud M A, Elumalai N K, Upama M B, Wang D, Zarei L, Goncales V R, Wright M, Xu C, Haque F and Uddin A 2018 Adsorbed carbon nanomaterials for surface and interface-engineered stable rubidium multi-cation perovskite solar cells *Nanoscale* **10** 773
[59] Li B, Rui Y C, Xu J L, Wang Y Q, Yang J X, Zhang Q H and Müller-Buschbaum P 2020 Solution-processed p-type nanocrystalline CoO films for inverted mixed perovskite solar cells *J. Colloid Interface Sci.* **573** 78
[60] Huang J, Yuan Y, Shao Y and Yan Y 2017 Understanding the physical properties of hybrid perovskites for photovoltaic applications *Nat. Rev. Mater.* **2** 17042
[61] Ball J M and Petrozza A 2016 Defects in perovskite-halides and their effects in solar cells *Nat. Energy* **1** 16149
[62] Pan D Y, Jiao J K, Li Z, Guo Y T, Feng C Q, Liu Y, Wang L and Wu M H 2015 Efficient separation of electron-hole pairs in graphene quantum dots by TiO_2 heterojunctions for dye degradation *ACS Sustain. Chem. Eng.* **3** 2405
[63] Yang D, Yang R, Wang K, Wu C, Zhu X, Feng J, Ren X, Fang G, Priya S and Liu S 2018 High efficiency planar-type perovskite solar cells with negligible hysteresis using EDTA-complexed SnO_2 *Nat. Commun.* **9** 3239
[64] Dong Q, Fang Y, Shao Y, Mulligan P, Qiu J, Cao L and Huang J 2015 Electron-hole diffusion lengths >175 μm in solution-grown $CH_3NH_3PbI_3$ single crystals *Science* **347** 967
[65] Berhe T A, Su W N, Chen C H, Pan C J, Cheng J H, Chen H M, Tsai M C, Chen L Y, Dubale A A and Hwang B J 2016 Organometal halide perovskite solar cells: degradation and stability *Energy Environ. Sci.* **9** 323